Metal oxide-promoted mesoporous silica as support for Ru-based CO_2 methanation catalysts

Plaifa Hongmanorom[a], Aurélien Neraud[b], Ales Styskalik[c], Wanwisa Limphirat[d], Piyasan Praserthdam[e], Damien P. Debecker[a,*]

[a] Institute of Condensed Matter and Nanosciences–Molecular, Solids and Reactivity (IMCN−MOST), Université Catholique de Louvain, Place Louis Pasteur, 1, box L4.01.09, 1348 Louvain-La-Neuve, Belgium

[b] Department of Chemistry and Applied Biosciences, ETH Zurich, Vladimir Prelog Weg 1−5, CH−8093 Zurich, Switzerland

[c] Department of Chemistry, Faculty of Science, Masaryk University, Kotlarska 2, Brno CZ-61137, Czech Republic

[d] Synchrotron Light Research Institute (Public Organization), 111 University Avenue, Muang, Nakhon Ratchasima, 30000, Thailand

[e] Center of Excellence on Catalysis and Catalytic Reaction Engineering (CECC), Department of Chemical Engineering, Faculty of Engineering, Chulalongkorn University, Bangkok 10330, Thailand

* Corresponding Author: damien.debecker@uclouvain.be

Abstract

Transition metals are widely employed to promote heterogeneous catalysts, yet their effects on Ru-based CO_2 methanation remain unclear. Herein, mesoporous silica supports promoted with Ti, Zr, Nb, or V were synthesized via an aerosol-assisted sol-gel process to systematically compare their effects. With fixed promoter (4 mol%) and Ru (2 wt%) loadings, V exhibits a unique promoting effect, attributed to Ru-V synergy that facilitates hydrogen spillover and generates oxygen vacancies. Increasing V loading to 16 mol% markedly reduces specific surface area and induces macropore formation due to V_2O_5 crystallization, yet significantly enhances activity, with CH_4 formation at 250 °C 8 times higher than unpromoted Ru/SiO_2. This improvement is rationalized by improved Ru dispersion and hydrogen spillover from Ru to adjacent V species. In-situ DRUV-Vis and XANES analyses reveal V^{5+} reduction to lower oxidation states and oxygen-vacancy generation, while in-situ DRIFTS shows modified CO adsorption, thereby promoting methanation via the CO pathway.

Keywords: Mesoporous silica; Promoter; Vanadium; Ruthenium; CO_2 methanation

1. Introduction

The hydrogenation of CO_2 with renewable hydrogen to produce methane is one of the promising approaches in CO_2 utilization strategies, as it has potential for both abatement of CO_2 and storage of renewable electric energy [1, 2]. Particularly in the Power-to-Gas (PtG) scenario, green hydrogen can be obtained from surplus renewable electricity (e.g., solar and wind-powered water electrolysis) and subsequently used to convert captured CO_2 into storable or transportable CH_4 through the existing natural gas pipeline infrastructure [3, 4].

The hydrogenation of CO_2 to CH_4, known as CO_2 methanation or Sabatier reaction, is an exothermic process, which is thermodynamically favorable at low temperatures. However, it is kinetically limited at mild temperatures due to the intrinsic stability of CO_2 [5, 6]. To achieve acceptable rate and selectivity, a highly active metal catalyst is required. Metals in groups 8-10 (e.g, Ru, Rh, Pd, Ni, Co and Fe) have been extensively studied for CO_2 methanation, and supported Ru catalysts are generally recognized as one of the most active and selective [7, 8]. A number of studies have shown that the catalytic activity and selectivity of Ru catalysts depend on various factors, such as Ru particle size and dispersion [9, 10], the type of support [11-13], structural/electronic effects in metal-support interactions [14-16] and the effects of metal promoters or doping [17-25].

Regarding the promoting/doping effects, alkali metals (Li, Na, K and Cs) are most frequently investigated for their influence on Ru methanation catalysts. The addition of alkali metals to Al_2O_3 [17], TiO_2 [18, 19] and ZrO_2 [20] has been found to improve the CO_2 methanation activity of Ru catalysts. It has been revealed that enrichment of electron density on Ru metals could enhance electron back-donation from Ru to adsorbed CO intermediates, which could then modify the nature and population of Ru carbonyls and facilitate their dissociative adsorption. In addition to alkali metals, alkali earth metals (Mg) [21], lanthanide (Ce) [22] and transition (Cr) [23] have also been reported to promote CO_2 methanation activity. For example, the improved activity of Ru/ZrO_2-MgO over Ru/ZrO_2 has been attributed to the modification of electronic properties: the incorporation of Mg^{2+} into the ZrO_2 lattice promoted the generation of oxygen vacancies, facilitating electron transfer from the associated oxygen vacancies/Zr^{3+} ($Zr^{4+} + e^-$ (O-vacancy) $\rightarrow$ Zr^{3+}) to interfacial adjacent Ru sites. This was shown to expedite both the decomposition of bidentate formate species and the subsequent breaking of carbonyl species for hydrogenation toward methane [21]. Likewise, the addition of CeO_2 to Ru/Al_2O_3 has been proposed to increase

the number of utilizable oxygen vacancies, leading to improved CO_2 reduction to CO via formate species before the successive CO methanation [22]. In another combined experimental and computational study, Cr^{3+} doping in the support of Ru/CeO_2 catalyst has been proposed to create more reactive surface oxygen vacancies and hydroxyl groups, which play crucial roles in the formation of bicarbonate and formate species. This, in turn, promoted the formate pathway, greatly improving the CO_2 methanation activity at low temperatures [23]. These aforementioned studies identify the origins of metal promotion/doping and highlight the importance of electronic metal-support interaction and oxygen vacancies in Ru catalysts for CO_2 methanation. Recently, we investigated the promotional effect of Ti on mesoporous silica-supported Ru catalysts for CO_2 methanation [26]. Ti-promoted mesoporous silica materials were prepared as supports via an aerosol-assisted sol-gel process (AASG), providing excellent Ti dispersion in the silica, even at high loadings. Using these model supports, it was found that Ti species play a marked beneficial role in stabilizing Ru nanoparticles and forming the interfacial contact between Ru and TiO_2. Importantly, the promotion of CO_2 activation and CO adsorption at the Ru-TiO_2 interfaces is responsible for the enhanced CO_2 methanation activity. It is therefore of interest to extend our studies to other transition metals from groups 4 and 5, for which very little is known regarding their effects on the CO_2 methanation activity and selectivity of Ru catalysts. To date, their promotional effects have been reported mainly for Ni-based methanation catalysts [27-30].

In the present study, we propose to leverage the AASG process (described in Fig. 1 and section 2.1.), modified from Smeets et al. [31] and Hongmanorom et al. [26], for the preparation of different metal oxide-promoted silica materials, including Ti, Zr, Nb, and V to unravel their effects on the catalyst properties and catalytic performance of silica-supported Ru catalysts in CO_2 methanation.

2. Experimental

2.1. Preparation of mesoporous metal oxide-promoted SiO_2 materials

As illustrated in Fig. 1, a series of mesoporous metal oxide-promoted SiO_2 materials were prepared using the AASG process, with the promoter loading set at 4 mol%. Tetrapropylammonium hydroxide (TPAOH, Merck, 40% w/w) was mixed with distilled water for 10 min. Tetraethyl orthosilicate (TEOS, Sigma, 98%) was then added as the silica precursor and vigorously stirred overnight to hydrolyse the silica precursor, followed by further aging at 70 °C for 15 h under

stirring. After that, pluronic F127 surfactant was added into the solution and thoroughly mixed at room temperature for 3 h to ensure complete dissolution. Metal alkoxide precursor was subsequently added dropwise and stirred overnight before aerosol spray drying. Titanium butoxide (Fluka, 99%), Zirconium butoxide (TCI, 80% in 1-butanol), Vanadium triisopropoxide oxide (Alfa Aesar, 96%), and Niobium n-butoxide (Alfa Aesar, 99%) were chosen as the metal alkoxide precursors. The molar ratio of the components was 1 Si: 0.042 M: 0.16 TPAOH: 0.005 F127: 21 H_2O, where M = Ti, Zr, V or Nb. A Büchi Mini Spray Dryer B-290 was used to aerosolize the precursor solution under 4-bar air pressure. The aerosol was carried by air through a glass chamber heated at 150 °C and pneumatically conveyed to a cyclone where the dried powder was collected. The obtained powder was further dried overnight in an oven at 70 °C and calcined in static air at 550 °C (5 °C/min) for 5 h. The materials were denoted as 4%M-SiO_2, where M = Ti, Zr, V or Nb. A series of mesoporous V-SiO_2 materials with different V loadings were also synthesized as described above, varying mol V / (mol V + mol Si) x 100% = 0, 4, 8, 12 and 16%. The materials were denoted as x%V-SiO_2, where x means mol% V loading.

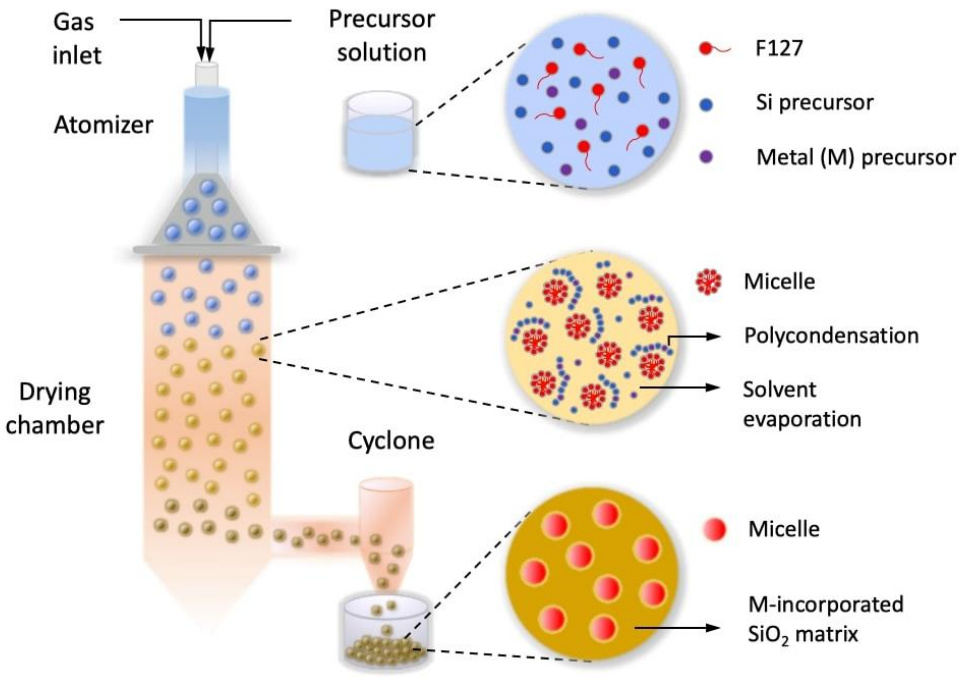

Fig. 1 Scheme of preparation of metal-incorporated silica microspheres via the AASG process. The precursor solution (TPAOH is not shown for clarity) is atomized into small droplets carried by air to pass through a heated zone of drying chamber. Under these conditions, solvent evaporation induces the self-assembly of F127 surfactant, forming micelles around which polycondensation of inorganic gel quickly occurs. The dried solid microspheres of metal-incorporated SiO_2 material are then collected after the cyclone prior to removal of surfactant by calcination. Further details are provided in the experimental section.

2.2. Preparation of RuO_2 catalysts

After the synthesis of support materials, 2 wt.% Ru-loaded catalysts were prepared by deposition of pre-synthesized RuO_2 nanoparticles onto silica supports. First, the RuO_2 colloidal suspension was prepared by dissolving 0.81 mmol of $RuCl_3$ into 40 mL of distilled water and subsequently adding 23 mL of aqueous hydrogen peroxide (14%) dropwise into the solution. After 5 min of stirring, the solution was incubated in an oven at 95 °C for 2 h. The obtained black RuO_2 colloidal suspension was cooled down to room temperature prior to mixing with 4 g of aerosol support under stirring at 50 °C for 16 h. Water was then evaporated by a rotavapor under vacuum at 50 °C. Finally, calcination was carried out at 450 °C (5 °C/min) for 16 h to obtain the catalyst denoted as Ru/x%M-SiO_2 (where M = Ti, Zr, V or Nb, and x is mol% of M loading).

2.3. Characterization

The details of the equipment, methods and procedures used for catalyst characterization (DRUV-vis, XRD, N_2-physisorption, ICP, TEM, H_2-TPR, CO_2-TPD, H_2 pulse chemisorption, XPS, XAS, DRIFTS) are provided in the Supporting Information.

2.4. Catalytic activity measurement

The catalytic activity measurement was performed in a continuous flow fixed-bed reactor. 100 mg catalyst was introduced in a 6 mm internal diameter Stainless steel tube and in-situ reduced at 200 °C for 1 h in a H_2 flow of 30 mL/min, followed by a 1 h purge with Ar flow of 10 mL/min. Afterward, a gas mixture containing 10% CO_2 and 40% H_2, diluted in Ar (total flow rate of 20 mL/min), was introduced. The reaction was evaluated at atmospheric pressure, using a stepwise temperature increase from 200 °C to 300 °C in 25 °C intervals. For each temperature, steady-state was ensured with at least four gas chromatography injections. The outlet gases were analyzed using a gas chromatograph (SCION 456-GC) equipped with Hayesep Q, Molsieve 5A, Porapak R and SCION-1 columns, a thermal conductivity detector (TCD for CO and CO_2) and a flame ionization

detector (FID for CH_4). All gas lines were maintained at 110 °C to prevent water condensation. CO_2 conversion (X_{CO_2}), CH_4 selectivity (S_{CH_4}), and CH_4 formation rate (r_{CH_4}) were calculated according to the following equations:

$$X_{CO_2}(\%) = \frac{F_{CO_{2,in}} - F_{CO_{2,out}}}{F_{CO_{2,in}}} \times 100\% \quad (1)$$

$$S_{CH_4}(\%) = \frac{F_{CH_{4,out}}}{F_{CO_{2,in}} - F_{CO_{2,out}}} \times 100\% \quad (2)$$

$$r_{CH_4}(mmol_{CH_4} g_{Ru}^{-1} s^{-1}) = \frac{F_{CH_{4,out}}}{m_{Ru}} \quad (3)$$

where F is the molar flow rate, and m_{Ru} is the mass of Ru measured by ICP-AES.

3. Results and discussion

3.1. Effect of metal promoter

3.1.1. Characterization of metal oxide-promoted (4%) silica supports and corresponding Ru catalysts

The metal (Ti, Zr, V or Nb)-promoted mesoporous SiO_2 supports were prepared by the AASG process with the promoter loading set at 4 mol%. The textural properties were evaluated by N_2 physisorption analyses. All samples exhibit type IV isotherm, which is the characteristic of mesoporous materials (Fig. 2a). The N_2 uptake at low relative pressure (P/P_0) is indicative of the presence of micropores. Pore size distributions of all samples, except 4%V-SiO_2, show the presence of mesopores in the range of *ca.* 10-30 nm (Fig. 2b). This is larger than the expected size of surfactant micelles (*ca.* 5-6 nm), and is attributed to the swelling effect of TPA^+ incorporation into the organic phase during the synthesis [32]. In the case of 4%V-SiO_2, the hysteresis loop appears at lower P/P_0, corresponding to smaller mesopores. The BET surface area (S_{BET}), total pore volume (V_p) and micropore volume (V_μ) are listed in Table 1. Interestingly, promoter-containing materials have higher S_{BET} and V_μ in comparison to pristine SiO_2. This could be due to the rearrangement of the silica network, forming crosslinks with the metal promoter, which has a larger ionic radius than Si^{4+} [33]. Additionally, irregularities in the pore structure could be formed as a result of differences in the polycondensation rates of Si and the metal promoter around micelles during the AASG synthesis. Consistently, the micropore volume is slightly higher for the metal-doped samples. After deposition of RuO_2 nanoparticles and subsequent calcination, the catalysts exhibit the same shape of type IV isotherms (Fig. S1(a)) and pore size distributions (Fig. S1(b)) with a slight decrease in

S_{BET}, V_p and V_μ (Table 1). Metal promoter and Ru contents measured from ICP-AES are consistently close to the nominal loadings (Table 2).

Table 1 Textural properties of mesoporous metal oxide-promoted silica materials and Ru catalysts.

Support	S_{BET} (m^2/g) [a]	V_p (cm^3/g) [b]	V_μ (cm^3/g) [c]	Catalyst	S_{BET} (m^2/g) [a]	V_p (cm^3/g) [b]	V_μ (cm^3/g) [c]
SiO_2	620	0.82	0.05	Ru/SiO_2	490	0.60	0.03
4%Ti-SiO_2	660	0.80	0.08	Ru/4%Ti-SiO_2	590	0.73	0.07
4%Zr-SiO_2	750	0.80	0.12	Ru/4%Zr-SiO_2	670	0.75	0.10
4%Nb-SiO_2	680	0.78	0.09	Ru/4%Nb-SiO_2	620	0.72	0.08
4%V-SiO_2	690	0.76	0.12	Ru/4%V-SiO_2	610	0.71	0.07
8%V-SiO_2	550	0.56	0.14	Ru/8%V-SiO_2	500	0.54	0.13
12%V-SiO_2	43	0.42	–	Ru/12%V-SiO_2	42	0.41	–
16%V-SiO_2	37	0.41	–	Ru/16%V-SiO_2	34	0.41	–

[a] The specific surface area (S_{BET}) was evaluated by Brunauer-Emmett-Teller (BET) method applied in a low range of relative pressure (P/P_0) from 0.01 to 0.1, taking the presence of micropores into account. [b] The total pore volume (V_p) was measured at $P/P_0 \sim 0.98$. [c] The micropore volume (V_μ) was estimated from the t-plot.

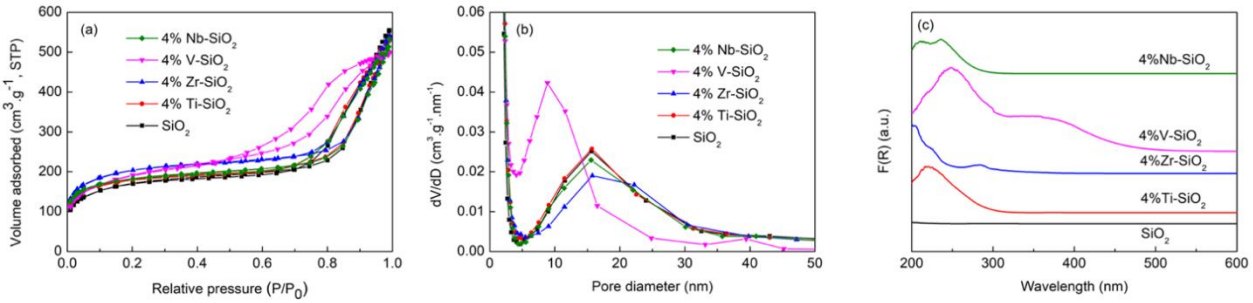

Fig. 2 (a) N_2 physisorption isotherms, (b) BJH pore-size distributions and (c) DRUV-visible spectra (Kubelka-Munk Function) of metal oxide-promoted SiO_2 supports.

The coordination geometry of metal promoter in silica material is investigated by DRUV-vis spectroscopy with pure silica as the reference. In Fig. 2(c), the DRUV-vis spectrum of 4%Ti-SiO_2 support displays a ligand-to-metal charge transfer (LMCT) band centered at about 220 nm, corresponding to tetrahedral TiO_4 species. In the 250-300 nm range, there is a small contribution from Ti in higher coordination (e.g., water-coordinated Ti species, one-dimensional polymerized TiO_4 and two-dimensional polymerized TiO_5) [31, 34]. No characteristic absorption band of octahedral TiO_6 at around 330 nm can be observed, indicating the absence of bulk TiO_2 nanocrystals [34, 35]. 4%Zr-SiO_2 support exhibits a strong absorption band at 205-215 nm, which can be assigned to the charge-transfer transition between O^{2-} and Zr^{4+} ions in tetrahedral coordination [36]. Relatively weak bands with the maximum at about 225 and 280 nm are also observable, suggesting the presence of multi-coordinated Zr^{4+} species (e.g., oligomers) and small ZrO_2 crystallites [37, 38]. In the case of 4%V-SiO_2 support, two main LMCT bands covering 200-300 nm and 300-410 nm are found. The former corresponds to isolated VO_x species and low-polymerized VO_x species in tetrahedral coordination, while the latter can be ascribed to highly polymerized VO_x species in tetrahedral and octahedral coordination [39, 40]. Besides, a very weak band (410-500 nm) attributed to octahedral vanadium species as in bulk-like V_2O_5 can be discerned [40, 41]. For 4%Nb-SiO_2 support, there are two main bands at 210 and 235 nm related to the presence of isolated NbO_4 and polymerized NbO_6 species, respectively, without the formation of bulk-type Nb_2O_5 located at 320 nm [42-44]. XRD analyses further reveal the amorphous feature of all aerosol 4%M-SiO_2 supports. The absence of crystalline phases in their XRD patterns (Fig. S1(c)) also suggests that crystalline clusters of metal promoter species are either absent or smaller than 3 nm. Taking DRUV-vis and XRD results together, metal promoters are thought to be mainly incorporated into the SiO_2 matrix and highly dispersed in the form of oligomeric/polymeric species. Homogeneous distribution of metal promoters over silica materials could also be observed by HAADF-STEM-EDS elemental mapping in Fig. S2.

Table 2 RuO_2 and Ru crystallite sizes, metal promoter (M) and Ru loadings, CH_4 formation rate at 250 °C of Ru catalysts supported on metal oxide-promoted silica and proportion of metallic Ru species after the reaction.

Catalyst	RuO_2 crystallite size (nm) [a]	Ru crystallite size (nm) [b]	ICP-AES		CH_4 formation rate ($mmol_{CH_4} g_{Ru}^{-1} s^{-1}$)	XPS (Spent) Ru^0/Ru^{tot}
			M (at.%)	Ru (wt.%)		
Ru/SiO_2	13.1	11.5	0.0	1.6	0.02	0.55
$Ru/4\%Ti\text{-}SiO_2$	11.6	8.7	3.7	1.8	0.03	0.57
$Ru/4\%Zr\text{-}SiO_2$	29.9	20.8	3.6	1.7	0.03	0.64
$Ru/4\%Nb\text{-}SiO_2$	11.4	9.0	3.7	1.8	0.03	0.57
$Ru/4\%V\text{-}SiO_2$	16.0	12.2	3.9	1.8	0.06	0.45
$Ru/8\%V\text{-}SiO_2$	16.4	13.0	7.9	1.6	0.05	0.35
$Ru/12\%V\text{-}SiO_2$	–	–	11.8	1.6	0.15	0.18
$Ru/16\%V\text{-}SiO_2$	–	–	16.0	1.6	0.17	0.16

[a] The RuO_2 crystallite size was obtained from the average between (110) and (101) planes of RuO_2 in the XRD patterns of freshly calcined catalysts using Scherrer equation.

[b] The Ru crystallite size was obtained from the average between (100) and (101) planes of Ru in the XRD patterns of spent catalysts using Scherrer equation.

In Fig. 3(a), the diffraction peaks of RuO_2 crystallites appear at $2\theta = 27.9°$ (110), 34.9° (101), 39.9° (200) and 54.0° (211) (JCPDS No. 43-1027), whereas the crystalline phase of the metal promoters are invisible in the XRD patterns. The RuO_2 crystallite sizes (calculated using the Scherrer equation) of $Ru/4\%Ti\text{-}SiO_2$ (11.6 nm) and $Ru/4\%Nb\text{-}SiO_2$ (11.4 nm) catalysts are smaller than those of Ru/SiO_2 catalyst without promoter (13.1 nm) (Table 2). In contrast, $Ru/4\%Zr\text{-}SiO_2$ (29.9 nm) and $Ru/4\%V\text{-}SiO_2$ (16.0 nm) catalysts contain much larger RuO_2 crystallites. However, HAADF-STEM-EDS mapping images (Fig. S2) reveal that Ru crystallites are non-uniformly distributed and aggregated on the Ru/SiO_2 catalyst surface. The presence of metal promoters appears to mitigate Ru aggregation to some extent, resulting in more homogenous dispersion of Ru nanoparticles in $Ru/4\%M\text{-}SiO_2$ catalysts. This discrepancy may be due to XRD detecting diffracting crystallite planes rather than entire particles [45]. Ru dispersion was also measured using H_2 pulse chemisorption (Table S1); however, the values are low, particularly for Ru/SiO_2

catalyst. Such underestimation has been previously reported in other studies, attributed to weak or slow kinetics of H_2 chemisorption [46, 47]. The reduction behavior of Ru catalysts was investigated using H_2-TPR technique (Fig. 3(b)). All catalysts, except Ru/4%V-SiO_2, exhibit one main TPR peak centered around 180-200 °C, corresponding to the reduction of oxidic Ru^{4+} to metallic Ru^0. Based on this observation, the reduction temperature at 200 °C was chosen and applied to all catalysts to ensure a fair comparison. An additional shoulder-like peak at 220 °C in the H_2-TPR profile of Ru/4%V-SiO_2 is likely associated with the reduction of V oxide facilitated by H_2 spillover from nearby Ru [48].

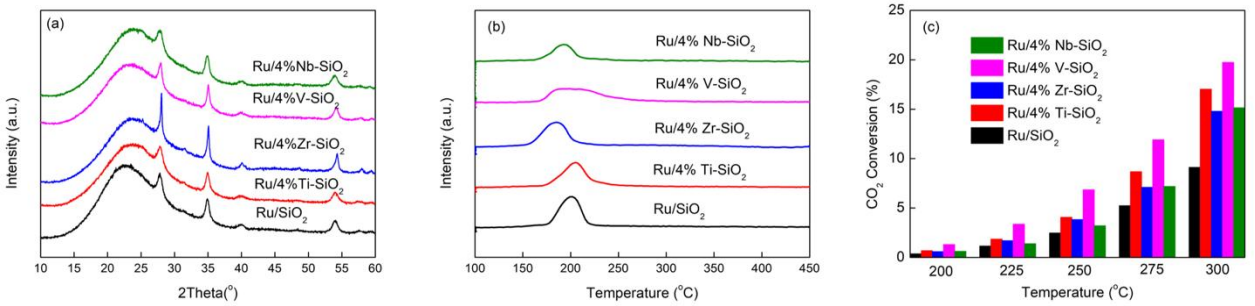

Fig. 3 (a) XRD patterns of freshly calcined Ru catalysts, (b) H_2-TPR profiles of Ru catalysts and (c) CO_2 conversion as a function of temperature (200-300 °C).

3.1.2. Catalytic performance of Ru catalysts supported on metal oxide-promoted (4%) silica materials

CO_2 methanation was evaluated from 200 to 300 °C. The reaction conditions were selected to obtain CO_2 conversion well below the thermodynamic limit, ensuring that the reported rates reflect the intrinsic activity. Under the given conditions, the selectivity to CH_4 remained at 100% across the entire temperature range for all catalysts. However, the level of activity is significantly influenced by the metal promoter (Fig. 3(c)). CO_2 conversion follows the trend: Ru/SiO_2 < Ru/4%Nb-SiO_2 ≈ Ru/4%Zr-SiO_2 < Ru/4%Ti-SiO_2 < Ru/4%V-SiO_2. The CH_4 formation rate at 250 °C, normalized by the Ru mass determined from ICP-AES, is shown in Table 2. Unpromoted, Ti-, Zr- and Nb-promoted catalysts exhibit comparable CH_4 formation rates in the 0.02-0.03 $\mathrm{mmol_{CH_4} g_{Ru}^{-1} s^{-1}}$ range, while V-promoted catalyst stands out with a higher rate of 0.06 $\mathrm{mmol_{CH_4} g_{Ru}^{-1} s^{-1}}$. Additionally, the apparent activation energies (E_a) derived from the Arrhenius plot (Fig. S3) are similar for Ru/SiO_2 (71.6 kJ/mol), Ru/4%Ti-SiO_2 (71.7 kJ/mol), Ru/4%Zr-SiO_2 (71.3 kJ/mol) and Ru/4%Nb-SiO_2 (72.5 kJ/mol), but clearly lower for Ru/4%V-SiO_2 (60.7 kJ/mol).

This decrease in E_a suggests that the nature of the active sites on Ru/4%V-SiO_2 may differ from those on the other catalysts, which may affect the CO adsorption energy or even the reaction mechanism (vide infra in the section 3.3.).

3.1.3. Characterization of spent Ru catalysts supported on metal oxide-promoted (4%) silica materials

After H_2 reduction and methanation reaction, the crystalline phases of metal promoters are still invisible in the XRD patterns (Fig. S4, top-left), indicating their good dispersion in the SiO_2 matrix. The diffraction peaks corresponding to RuO_2 crystallites disappear from the XRD patterns, replaced by emerging diffraction peaks of metallic Ru at 38.8° (100), 42.0° (002) and 43.8° (101) (JCPDS No. 06-0663). The Ru crystallite sizes estimated using the Scherrer equation (Table 2) are smaller than the corresponding RuO_2 crystallite sizes due to the shrinkage that occurs during the reduction from RuO_2 to metallic Ru.

The Ru chemical state and surface composition after the reaction was also investigated by XPS (Fig. S4, with details of the XPS spectra treatment and processing). Three deconvoluted components (metallic Ru, oxidized Ru^{4+} and C 1s) are tabulated in Fig. S4. A doublet at 279.8 ± 0.1 eV with an asymmetric shape is associated to Ru in metallic state, whereas a main doublet at 280.6 ± 0.1 eV accompanied by a satellite doublet at 282.5 ± 0.1 eV is attributed to the oxidized Ru^{4+} species [49]. The ratio of surface metallic Ru is comparable among Ru/SiO_2, Ru/4%Ti-SiO_2 and Ru/4%Nb-SiO_2, with relatively higher proportions on Ru/4%Zr-SiO_2 and lower proportions on Ru/4%V-SiO_2 (Table 2). This trend aligns with the reducibility of the RuO_2 phase, as shown in H_2-TPR profiles (Fig. 3(b)).

3.2. Effect of V loading

Building on the finding that V was the most promising promoter, we further investigated the effect of V loading (4, 8, 12 and 16%) on the catalyst properties and catalytic performance of Ru/V-SiO_2 catalysts.

3.2.1. Characterization of V-promoted silica supports and corresponding Ru catalysts

The textural properties change significantly with increasing V loading (Fig. 4(a)). The inflection point in the isotherms shifts to a lower relative pressure as V loading increases to 8%, corresponding to smaller mesopore diameter (Fig. 4(b)). Further increasing V loading to 12% and

16% leads to substantial reduction in S_{BET} and V_p (Table 1). Additionally, micropores disappear replaced by the formation of macropores (Fig. 4(b)). Likewise, the morphology modifications with increasing V loading are visible in TEM images of Ru/V-SiO_2 catalysts (Fig. 5(a-d)). Catalysts containing 4% and 8%V exhibit a spherical morphology with mesopores, while those with 12% and 16%V display an irregular shape with macropores. After deposition of RuO_2 nanoparticles and subsequent calcination, isotherms (Fig. S5(a)) and pore size distributions (Fig. S5(b)) remain similar for all catalysts, with slight decrease in S_{BET}, V_p and V_μ observed for Ru/4%V-SiO_2 and Ru/8%V-SiO_2 catalysts (Table 1). The significant changes in textural properties with increasing V loading can be attributed to the formation of V_2O_5 crystallites, as revealed by the DRUV-vis and XRD results discussed below.

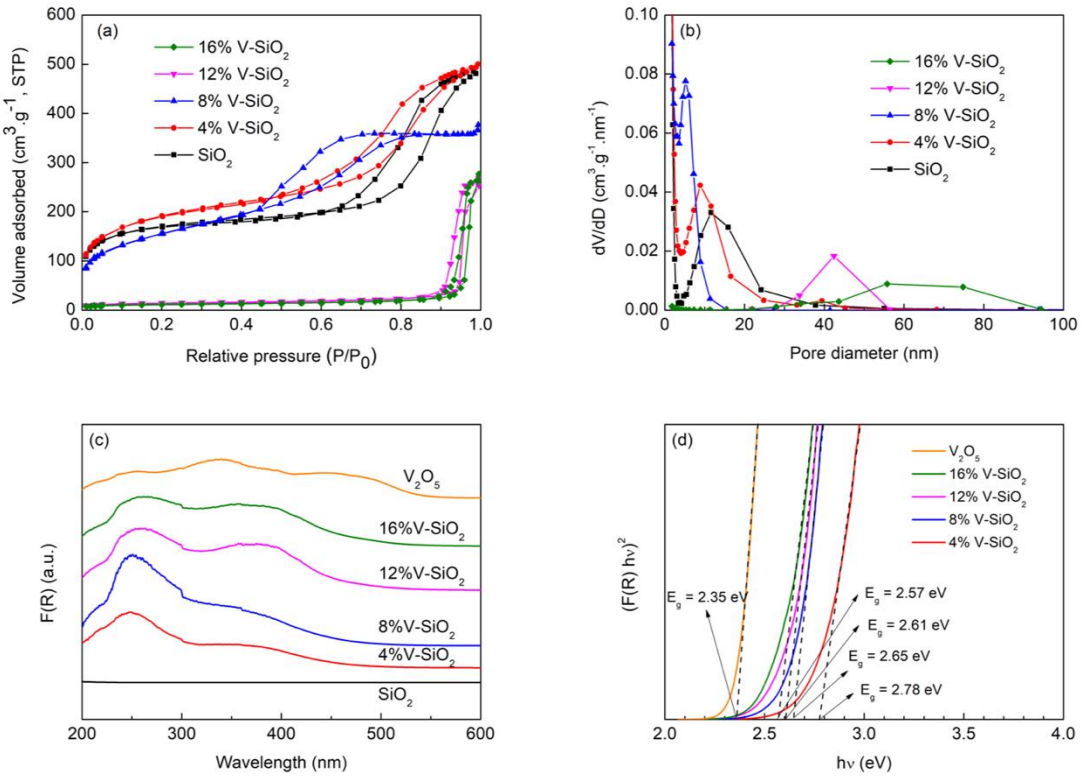

Fig. 4 (a) N_2 physisorption isotherms, (b) BJH pore-size distributions, (c) DRUV-visible spectra (Kubelka-Munk function) of V-promoted SiO_2 supports with different V loadings and (d) Band gap energy (E_g) for metal oxide-promoted SiO_2 supports from the optical absorption edges. F(R) and hν are the Kubelka-Munk function and the incident photon energy, respectively.

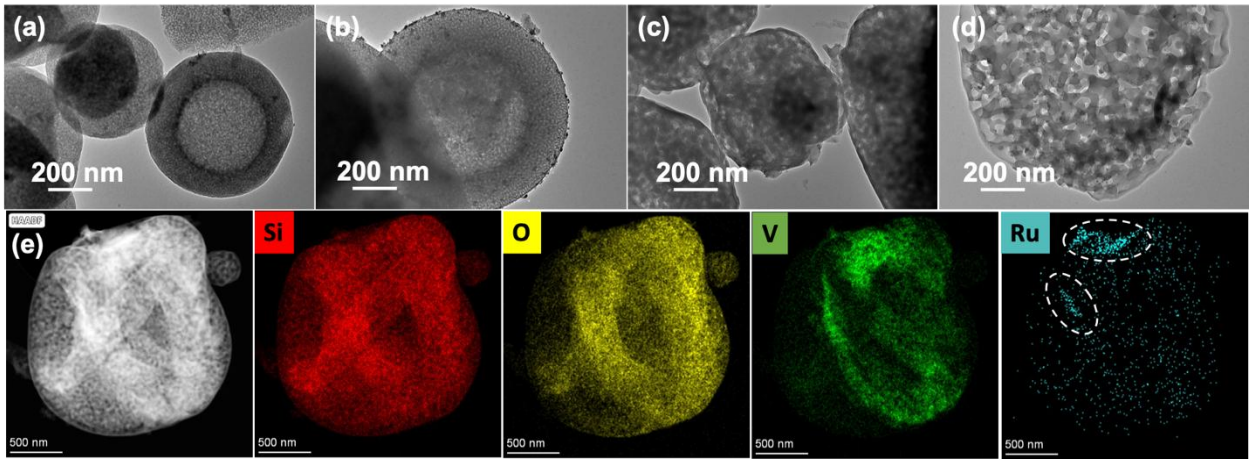

Fig. 5 TEM images of reduced (a) Ru/4%V-SiO_2, (b) Ru/8%V-SiO_2, (c) Ru/12%V-SiO_2 and (d) Ru/16%V-SiO_2 catalysts. (e) HAADF-STEM-EDS mapping images of reduced Ru/16%V-SiO_2 catalyst.

The coordination environment of vanadium in V-SiO_2 supports with varying V loadings is identified from Fig. 4(c), using V_2O_5 (obtained from calcination of ammonium metavanadate, NH_4VO_3, at 550 °C) as a reference. When V loading is higher than 4%, the band above 410 nm, ascribed to octahedrally coordinated bulk-like VO_x species, becomes more prominent. The absorption edge energy (E_g) is further determined from the Kubelka-Munk function to evaluate the polymerization degree of VO_x species. As reported, sodium meta-vanadate ($NaVO_3$, V^{5+}), a standard for linearly polymerized tetrahedral units, has the E_g value of 3.16 eV [50]. From Fig. 4(d), the estimated E_g values of V-SiO_2 supports lie between those of $NaVO_3$ and V_2O_5 (2.35 eV) and decrease with increasing V loading, reflecting a higher ratio of octahedrally coordinated bulk-like VO_x species and high-polymerized VO_x species to low-polymerized and isolated VO_x species. XRD analysis (Fig. 6(a)) corroborates that at high V loadings (12% and 16%), orthorhombic crystalline phases of V_2O_5 appear (JCPDS No. 41-1426). Elemental mapping of Ru/16%V-SiO_2 catalyst in Fig. 5(e) reveals V-rich regions, which can also be observed for Ru/12%V-SiO_2 catalyst (Fig. S6). Despite the presence of these V-rich regions, no separated V_2O_5 phases are detected that are not in contact with the silica support.

After the addition of RuO_2 nanoparticles, diffraction peaks of RuO_2 at $2\theta = 27.9°$, 34.9°, 39.9° and 54.0° (JCPDS No. 43-1027) are observed, with no V_2O_5 crystalline phases detected for Ru/4%V-SiO_2 and Ru/8%V-SiO_2 catalysts (Fig. 6(b)). Much broader RuO_2 peaks, overlapping with V_2O_5 peaks, are evident for Ru/12%V-SiO_2 and Ru/16%V-SiO_2 catalysts, indicating smaller RuO_2

crystallites (< 5 nm) in the presence of V_2O_5 crystal structure. This observation aligns with the increased Ru dispersion determined for Ru/12%V-SiO_2 (5.9%) and Ru/16%V-SiO_2 (8.3%) catalysts (Table S1), despite the underestimation of Ru dispersion by H_2 pule chemisorption. The reduction behavior of Ru/V-SiO_2 catalysts is also clearly influenced by V loading, as shown in Fig. 6(c). The high-temperature peak above 600 °C, ascribed to the reduction of polymeric V^{5+} species, gradually shifts to higher temperature with increasing V loading. Similarly, the low-temperature peak corresponding to Ru^{4+}-to-Ru^0 reduction at 200 °C shifts progressively to higher temperatures. For Ru/4%V-SiO_2 and Ru/8%V-SiO_2 catalysts, two overlapping low-temperature peaks are observed, likely caused by interactions between RuO_2 and V promoter. In contrast, for Ru/12%V-SiO_2 and Ru/16%V-SiO_2 catalysts, the overlap vanishes and is accompanied by the emergence of shoulder peaks between 300-600 °C, which are absent in the H_2-TPR profile of the bare 16%V-SiO_2 support (Fig. S7 and the corresponding discussion). These broad reduction profiles suggest the strong interaction between Ru and VO_x species, where some Ru nanoparticles preferentially interact with V-enriched regions (indicated by white dashed ellipses in Fig. 5(e)). Hydrogen spillover from Ru could therefore facilitate the reduction of nearby VO_x from V^{5+} to V^{4+} and/or V^{3+} [48].

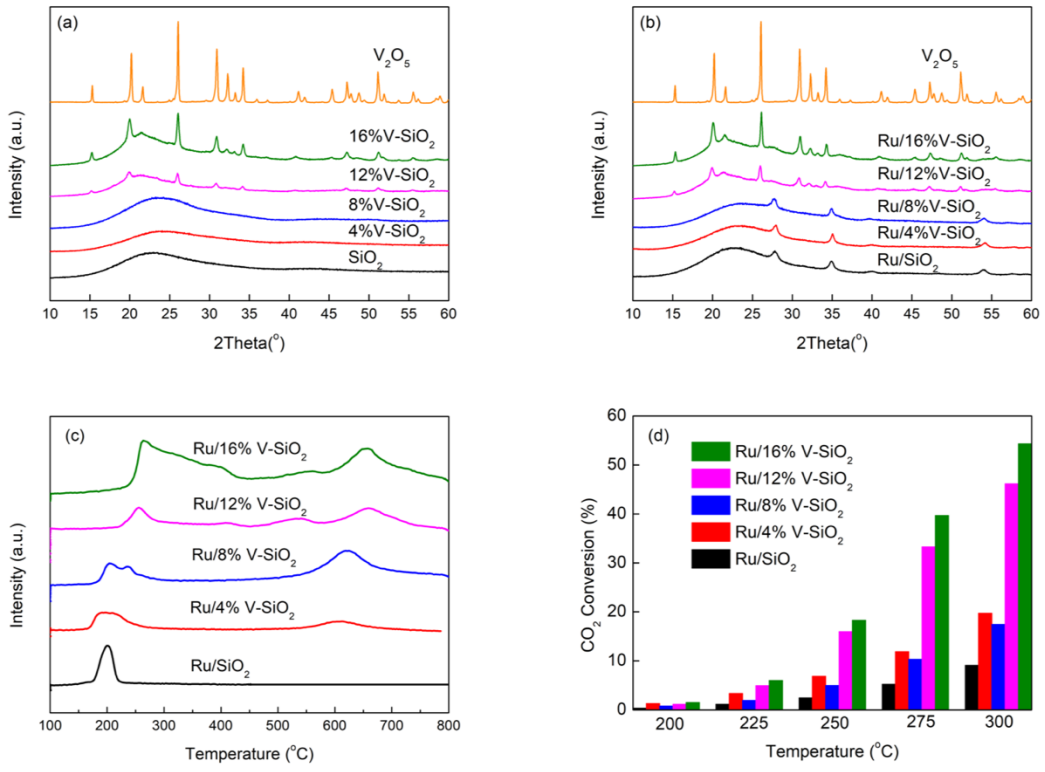

Fig. 6 XRD patterns of (a) V-promoted SiO_2 supports and (b) freshly calcined Ru/V-SiO_2 catalysts with V_2O_5 as a reference. (c) H_2-TPR profiles of Ru/SiO_2 and Ru/V-SiO_2 catalysts and (d) CO_2 conversion as a function of temperature (200-300 °C).

3.2.2. Catalytic performance of Ru catalysts supported on V-promoted silica materials

Increasing V loading from 4% to 8%, the catalytic activity was essentially maintained (slight decrease, possibly attributed to slightly lower Ru dispersion, see Table S1). Although further increasing V loading to 12% and 16% results in substantial decrease in specific surface area and the formation of macropores due to V_2O_5 crystallite buildup, the catalytic activity over Ru/12%V-SiO_2 and Ru/16%V-SiO_2 catalysts is strikingly improved, while maintaining 100% CH_4 selectivity across the entire temperature range (Fig. 6(d)). The CH_4 formation rate at 250 °C of Ru/16%V-SiO_2 (0.17 $\mathrm{mmol_{CH_4} g_{Ru}^{-1} s^{-1}}$) catalyst is ca. 8-fold higher than that of Ru/SiO_2 (Table 2), showing that high surface area is not the key factor for these catalysts. Rather, V_2O_5 helps stabilizing Ru nanoparticles and prevents their aggregation, thereby leading to higher Ru dispersion. To validate that Ru is the active metal and V acts solely as a promoter, the catalytic test was also performed over 16%V-SiO_2 support. Only a trace amount of CH_4 detected at 300 °C (as expected, owing to the poor ability of VO_x to dissociate H_2 in the 200-300 °C range), confirming that the enhanced activity of Ru/16%V-SiO2 catalyst arises from Ru-V interactions rather than from an additive effect of Ru and VO_x species.

The CH_4 formation rate of Ru/16%V-SiO_2 is also compared with that of other catalysts reported in the literature (Table S2). Ru/16%V-SiO_2 outperforms other Ru-based catalysts supported on silica materials and exhibits CH_4 formation rate comparable to that of Ru-based catalysts supported on metal-oxides. Additionally, the apparent activation energy (E_a) derived from the Arrhenius plot (Fig. S8(a)) increases from 60.7 kJ/mol for Ru/4%V-SiO_2 to 70.5 kJ/mol, 99.2 kJ/mol and 94.7 kJ/mol for Ru/8%V-SiO_2, Ru/12%V-SiO_2 and Ru/16%V-SiO_2, respectively. The higher E_a values for Ru/12%V-SiO_2 and Ru/16%V-SiO_2 coincide with the lower reducibility of RuO_2, as indicated by H_2-TPR results ((Fig. 6(c)). When pre-reduced at 300 °C instead of 200 °C, a larger fraction of RuO_2 in Ru/16%V-SiO_2 is converted to metallic Ru. As a result, CO_2 conversion of Ru/16%V-SiO_2 at low temperatures increases significantly. Correspondingly, the E_a value of Ru/16%V-SiO_2 pre-reduced at 300 °C (57.9 kJ/mol) becomes comparable to that of Ru/4%V-SiO_2 (55.7 kJ/mol) (Fig. S8(b)). This suggests a similar nature of active sites and reaction mechanism over these two

catalysts (vide infra in the section 3.3.). The Ru/16%V-SiO_2 catalyst underwent a stability test at 300 °C for 40 h. The CH_4 selectivity remained at 100%, with a decrease in CO_2 conversion of less than 5% over the 40-hour runtime (Fig. S9(a)).

We attempted to further increase the V loading beyond 16% using the AASG process; however, gel quickly formed during the precursor solution preparation, hindering the aerosol spray drying. We also prepared Ru catalyst supported on 16%V-SiO_2 via two-step impregnation, referred to as Ru/16%V-SiO_2 IM (Fig. S9(b), with preparation details provided). The Ru/16%V-SiO_2 catalyst synthesized via the AASG method followed by Ru deposition outperforms the Ru/16%V-SiO_2 IM catalyst, highlighting the effectiveness of the AASG process in preparing metal oxide-promoted silica supports for Ru catalysts. Furthermore, Ru catalyst supported on V_2O_5 was prepared (Fig. S9(b) with preparation details provided), and Ru/V_2O_5 achieved CO_2 conversion comparable to Ru/16%V-SiO_2 catalyst. Notably, V_2O_5 is an unconventional support for CO_2 methanation, but our finding confirms that V_2O_5 can serve as a good support for Ru-based CO_2 methanation catalysts.

3.2.3 Characterization of spent Ru catalysts supported on V-promoted silica materials

After exposure to H_2/Ar at 200 °C and CO_2/H_2/Ar at 200-300 °C, the diffraction peaks related to V_2O_5 in Ru/12%V-SiO_2 and Ru/16%V-SiO_2 catalysts disappear, while broad peaks at 36° and 54° emerge, corresponding to corundum V_2O_3 (Fig. S10, top-left, JCPDS No. 34-0187) [51, 52]. It is likely that hydrogen spillover from Ru during H_2 reduction and CO_2 hydrogenation facilitates the reduction of V_2O_5, transforming crystalline V_2O_5 into VO_2 and further into corundum V_2O_3 through phases that are nearly X-ray amorphous [52]. This phase transformation is confirmed by in-situ DRUV-vis and in-situ XANES measurements (vide infra). Despite the structural transformation, vanadium species could still stabilize Ru nanoparticles and prevent their aggregation, inferred from much broader metallic Ru peaks at 38.8°, 42.0° and 43.8° in the XRD patterns of Ru/12%V-SiO_2 and Ru/16%V-SiO_2 compared to the other three catalysts.

The surface Ru composition of the spent catalysts investigated by XPS is shown in Fig. S10 and Table 2. It is evident that the ratio of surface metallic Ru decreases with increasing V loading. This trend is clearly associated with the reducibility of Ru catalysts, as presented in H_2-TPR profiles (Fig. 6(c)), where Ru/12%V-SiO_2 and Ru/16%V-SiO_2, in particular, are reducible at higher temperatures. Fig. S10 also displays XPS spectra of the O 1s and V 2p binding energies for the spent catalysts. In the O 1s region, the peak at 532.7 eV attributed to hydroxyl groups and

oxygenated carbon species is dominant for all samples, while the peak at 530.3 eV related to lattice oxygen of V_2O_5 is noticeable for spent Ru/12%V-SiO_2 and Ru/16%V-SiO_2 [16, 53]. Correspondingly, in the V 2p region, the V $2p_{3/2}$ peak is blue-shifted with increasing V loading: Ru/4%V-SiO_2 (516.5 eV) < Ru/8%V-SiO_2 (516.8 eV) < Ru/12%V-SiO_2 (517.3 eV) < Ru/16%V-SiO_2 (517.5 eV), as binding energies of ca. 516.5 and 517.5 eV are characteristic for V^{4+}(VO_2) and V^{5+}(V_2O_5), respectively [54, 55]. However, XPS measurements were carried out ex-situ. The spent catalysts were inevitably exposed to air for a short period, leading to the re-oxidation of V species. More information on the formation of V^{4+}/V^{3+} and oxygen vacancies could be obtained from the in-situ experiments below.

3.3. In-situ DRUV-Vis, XANES, and DRIFTS experiments to elucidate the promoting effect of V

Among Ti, Zr, Nb, and V, V is identified as the most promising promoter. The superior promoting effect of V in Ru-based catalysts may tentatively be attributed to its intrinsic redox properties: V can exist in multiple oxidation states (V^{2+}, V^{3+}, V^{4+}, and V^{5+}), enabling dynamic redox interactions with Ru [56, 57]. The reduction of V species can be facilitated through hydrogen spillover from adjacent Ru sites, which in turn promotes the formation of surface oxygen vacancies.

In this section, in-situ experiments were conducted primarily on Ru/16%V-SiO_2 catalyst (with some also performed on Ru/SiO_2 and Ru/4%V-SiO_2 catalysts for comparison) to investigate the presence of V^{4+}/V^{3+} and oxygen vacancies, as well as their role in the significant enhancement of activity during CO_2 methanation.

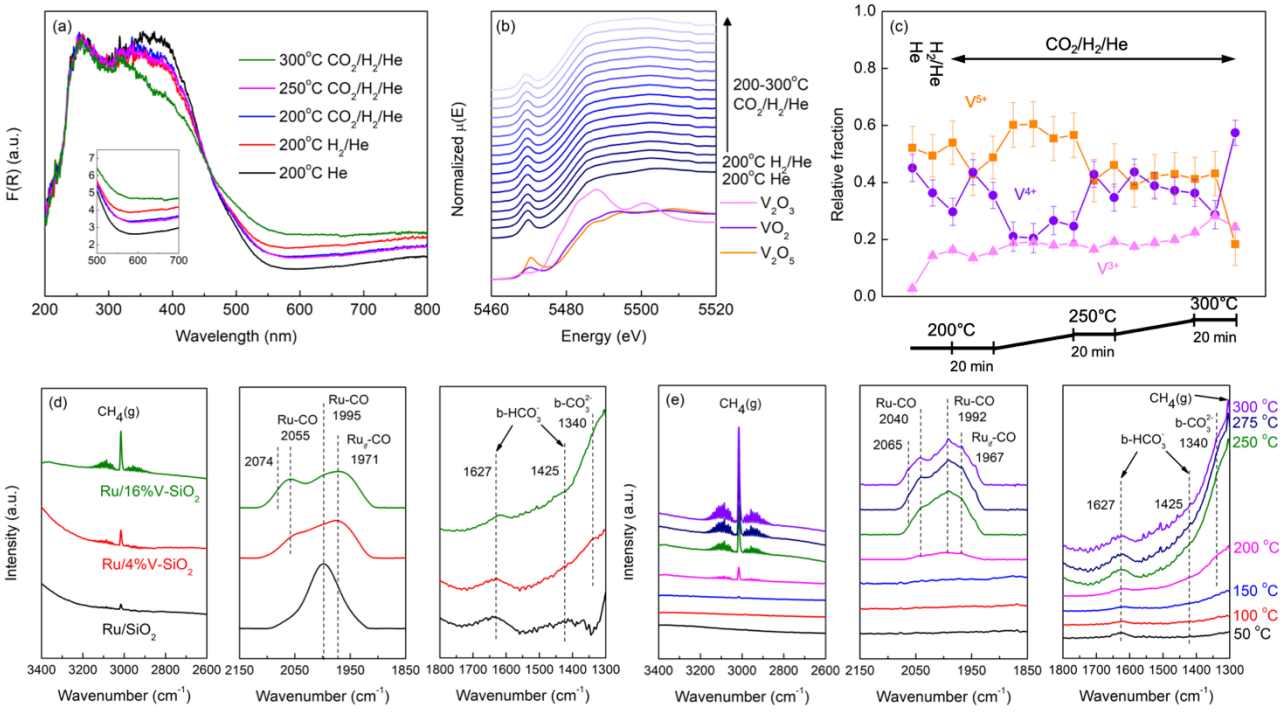

Fig. 7 (a) In-situ DRUV-Vis spectra (inset highlighting the 500-700 nm range with an intensity scale) of Ru/16%V-SiO_2 catalyst during H_2 reduction at 200 °C and CO_2 methanation at 200-300 °C. (b) In-situ V K-edge XANES spectra of vanadium standards (V_2O_5, VO_2 and V_2O_3) and Ru/16%V-SiO_2 catalyst during H_2 reduction at 200 °C and CO_2 methanation at 200-300 °C. (c) Relative fractions of the V^{5+}, V^{4+}, and V^{3+} components obtained from linear combination fitting of in-situ V K-edge XANES spectra in (b). (d) In-situ DRIFTS spectra during CO_2 methanation at 250 °C after 30 mins over Ru/SiO_2, Ru/4%V-SiO_2, and Ru/16%V-SiO_2 catalysts. (e) In-situ DRIFTS spectra recorded at steady-state during CO_2 methanation from 50 °C to 300 °C over Ru/16%V-SiO_2 catalyst.

The in-situ DRUV-vis spectra of Ru/16%V-SiO_2 during H_2 reduction at 200 °C and CO_2 methanation at 200-300 °C are presented in Fig. 7(a). The intensity of the LMCT bands in the 300-500 nm region, corresponding to high-polymerized VO_x species and bulk-like V_2O_5, decreases upon exposure to H_2/He at 200 °C. Simultaneously, a broad and weak band emerges in the 500-700 nm region, attributed to the d-d transition of V^{4+} and/or V^{3+} species, indicating the reduction of V^{5+} to V^{4+} or V^{3+} [58, 59]. According to the literature, the reduction of bulk V_2O_5 (via V_4O_9 and V_6O_{13}) to a mixture of VO_2 and V_2O_3 begins at approximately 500 °C under hydrogen [52, 60]. With Ru present in Ru/16%V-SiO_2 catalyst, this reduction can occur at a significantly lower temperature due to hydrogen spillover from Ru nanoparticles. When exposed to CO_2/H_2/He at 200 and 250 °C, the band at 500-700 nm slightly decreases. At higher temperature (300 °C), the band

at 300-500 nm noticeably decreases accompanied by an increase of the band at 500-700 nm. The more pronounced reduction at 300 °C corresponds to the first main peak observed in H_2-TPR profile of Ru/16%V-SiO_2 catalyst (Fig. 6(c)). The intensity of the LMCT band in the 200-300 nm region, corresponding to isolated and low-polymerized VO_x species, remains unchanged. It has been reported that V_2O_5 and polyvanadate species are more easily reduced than monovanadate species [59].

In-situ XANES provides deeper insight into changes in the oxidation states of vanadium. Fig. 7(b) shows in-situ V K-edge XANES spectra of vanadium standards (V_2O_5, VO_2 and V_2O_3, representing V^{5+}, V^{4+} and V^{3+}, respectively) and Ru/16%V-SiO_2 catalyst during reductive pretreatment and CO_2 hydrogenation. Linear combination fitting (LCF; fit range 5606–5706 eV; E0 not allowed to float; fit forced to get the sum of one) was used to determine the relative fractions of V^{5+}, V^{4+} and V^{3+}, as shown in Fig. 7(c). The LCF result is fit within R factor < 0.05. It should be noted that crystalline standards were used, while Ru/16%V-SiO_2 consists of VO_x species dispersed on SiO_2. To account for this uncertainty in vanadium speciation, error bars corresponding to the square root of the reduced chi-square calculated by Athena were also included. Under H_2/He at 200 °C, V^{5+} and V^{4+} are partly reduced to V^{3+}. With the introduction of CO_2 (CO_2/H_2/He) between 200 and 250 °C, a portion of V^{4+} is oxidized back to V^{5+}. Further reduction of V^{5+} to V^{4+} and V^{3+} continues above 250 °C. After 20 min at 300 °C, V_2O_5 is largely transformed to V^{4+}, with some fraction further reduced to V^{3+}. For Ru/4%V-SiO_2 (Fig. S11 (a) and (b)), V^{5+} is mainly reduced to V^{4+} under H_2/He at 200 °C, while the presence of V^{3+} becomes noticeable at higher temperature above 250 °C. The ratio of $\frac{(V^{3+}+V^{4+})}{(V^{3+}+V^{4+}+V^{5+})}$ derived from Fig. 7(c) and Fig. S11 (b) is also presented in Fig. S11 (c). The temperature-dependent evolution of vanadium oxidation states demonstrates that vanadium species in Ru/16%V-SiO_2 undergo greater and deeper reduction than those in Ru/4%V-SiO_2, suggesting a higher concentration of oxygen vacancy formation.

In-situ DRIFTS experiments under CO_2/H_2/He mixture were performed to probe the formation of surface intermediate species and to further understand the role of vanadium and oxygen vacancies. Fig. 7(d) displays in-situ DRIFTS spectra during CO_2 methanation at 250 °C after 30 mins over Ru/SiO_2, Ru/4%V-SiO_2, and Ru/16%V-SiO_2 catalysts. The band at 3017 cm^{-1} corresponds to gaseous CH_4. Consistent with catalytic activity, this band is significantly more intense for Ru/16%V-SiO_2 than for Ru/4%V-SiO_2 and Ru/SiO_2. Additionally, a marked difference is observed

in the carbonyl band region (2150-1850 cm^{-1}) between Ru/SiO_2 and $Ru/V\text{-}SiO_2$ catalysts. For Ru/SiO_2, only the band ascribed to CO linearly adsorbed on Ru sites (Ru-CO at 1995 cm^{-1}) is present, whereas three additional bands appear for $Ru/V\text{-}SiO_2$ catalysts. The bands at 2055 cm^{-1} and 1971 cm^{-1} can be attributed to linearly bonded CO on Ru sites (Ru-CO) and bridged CO at the metal-support interface (Ru_{if}-CO), respectively [15]. The higher wavenumber of the Ru-CO band could be indicative of higher CO coverage [61]. Additionally, the formation of oxygen vacancies in $Ru/V\text{-}SiO_2$ may enhance electron transfer from the associated oxygen vacancies to adjacent Ru sites at the interface, leading to an increased electron density at the Ru-support interface [21]. This shift in electron distribution could modify CO adsorption from linear CO adsorption on Ru sites toward bridged CO adsorption at interfacial sites [20, 62]. An alternative explanation for the emergence of bridged CO could be the improved Ru dispersion observed in $Ru/V\text{-}SiO_2$ catalysts, as smaller Ru particles expose a larger fraction of interfacial sites. Nevertheless, comparison of in-situ DRIFTS spectra of $Ru/4\%V\text{-}SiO_2$ and $Ru/4\%Ti\text{-}SiO_2$ (Fig. S12), which possess comparable Ru dispersions, shows that the differences in CO adsorption modes persist. Although the influence of Ru dispersion on CO adsorption cannot be entirely ruled out, this comparison suggests that the formation of oxygen vacancies associated with V^{5+} reduction predominantly accounts for the appearance of bridged CO. The assignment of the shoulder-like band at 2074 cm^{-1} remains uncertain in the literature. It has been attributed either to linear/multi-carbonyl species adsorbed on partially oxidized Ru sites ($Ru^{\delta+}\text{-}(CO)_n$, n = 1-3), typically accompanied by the band at 2140-2100 cm^{-1}) [15, 63], or to linear CO adsorbed on Ru sites of monolayer Ru islands on the support [25, 64]. Due to the absence of high-frequency bands at 2140-2100 cm^{-1}, we infer that the primary contributor is CO linearly adsorbed on monolayer Ru sites. The carbonate region also differs between Ru/SiO_2 and $Ru/V\text{-}SiO_2$ catalysts. Besides the bands associated with bidentate bicarbonate (b-HCO_3^-) at 1627 and 1425 cm^{-1}, the band related to bidentate carbonate (b-CO_3^{2-}) at 1340 cm^{-1} is more prominent for $Ru/V\text{-}SiO_2$ catalysts [21, 65]. The formation of bidentate carbonate could result from CO_2 adsorption on strong basic sites of V-promoted catalysts, whose presence was evidenced by CO_2-TPD analysis (Fig. S13 with a detailed description in the Supporting Information). In-situ DRIFTS spectra during CO_2 methanation over $Ru/16\%V\text{-}SiO_2$ (Fig. 7(e)) show an increase in b-HCO_3^- and b-CO_3^{2-} band intensities with increasing temperature from 50 °C to 300 °C. No formate species are observed, indicating that bicarbonate/carbonate species are not further hydrogenated toward CH_4 formation via the formate route. Instead, the adsorbed CO_2 is converted into carbonyl

species through the decomposition of b-HCO_3^- or the direct dissociation of CO_2. These CO_2 adsorption and activation steps could be promoted by a high concentration of oxygen vacancies. Carbonyl species and gaseous CH_4 begin to form at 200 °C and significantly increase between 250-300 °C, correlating with a higher concentration of oxygen vacancies, as indicated by $\frac{(V^{3+}+V^{4+})}{(V^{3+}+V^{4+}+V^{5+})}$ ratio in Fig. S11(c). Overall, the current findings are consistent with CO_2 methanation on Ru/SiO_2 and $Ru/V\text{-}SiO_2$ catalysts proceeding via the CO pathway. During H_2 reduction and CO_2 hydrogenation, dissociated H atoms could spill over from Ru sites to nearby V species, synchronously generating V^{4+}/V^{3+} and surface oxygen vacancies. These surface oxygen vacancies could facilitate electron transfer to interfacial Ru sites and subsequent electron back-donation from interfacial Ru sites to the adsorbed CO, thereby weakening the C-O bond for further hydrogenation toward CH_4 formation [20, 21, 66].

4. Conclusions

Mesoporous metal oxide-promoted silica materials (4%M-SiO_2, where M = Ti, Zr, Nb or V) with high specific surface area and large pores were successfully synthesized using the aerosol-assisted sol-gel process. XRD, DRUV-Vis and HAADF-STEM-EDS analyses confirm the homogenous distribution of Ti, Zr, Nb and V species in these supports. Ru-based catalysts were then prepared by deposition of preformed RuO_2 nanoparticles onto the metallosilicate supports. Compared to the unpromoted Ru catalyst (Ru/SiO_2), 4%metal oxide-promoted Ru catalysts exhibit higher CH_4 formation rate, as the metal promoters help mitigate Ru aggregation to some extent. More importantly, the interaction between Ru and V species provides a distinct promotional effect, making $Ru/4\%V\text{-}SiO_2$ catalyst standing out among the 4%metal oxide-promoted Ru catalysts in terms of CH_4 formation rate. Further increasing V loading up to 16% results in substantial reduction in specific surface area and the formation of macropores, attributed to V_2O_5 crystallite buildup. Despite these changes, $Ru/16\%V\text{-}SiO_2$ exhibits a dramatically enhanced catalytic activity, with its CH_4 formation rate at 250 °C being ca. 8-fold higher than that of pristine Ru/SiO_2. In-situ DRUV-Vis and in-situ XANES measurements reveal that hydrogen spillover from Ru sites facilitates the reduction of nearby V species from V^{5+} to V^{4+} and V^{3+}, synchronously generating surface oxygen vacancies. As evidenced by in-situ DRIFTS, these vacancies alter the nature of Ru carbonyls from linear CO adsorption on Ru sites (as in Ru/SiO_2) to bridged CO adsorption at interfacial sites (as in $Ru/V\text{-}SiO_2$), thereby enhancing CO_2 methanation activity via the CO pathway. This study

highlights the versatility and effectiveness of the aerosol-assisted sol-gel process while uncovering a unique promotional effect of V in Ru-based catalysts for enhanced CO_2 methanation performance.

Acknowledgement

This work has been supported by the Southeast Asia-Europe Joint Funding Scheme for Research and Innovation (Project PINT-MULTI/BEJ – R.8001.21). Additional funding was provided by the NSRF via the Program Management Unit for Human Resources & Institutional Development, Research and Innovation [Grant number B16F640034]. We extend our gratitude to CF CryoEM of CIISB, Instruct-CZ Centre, supported by MEYS CR (LM2023042)) and European Regional Development Fund-Project „UP CIISB“ (No. CZ.02.1.01/0.0/0.0/18_046/0015974). The authors sincerely thank Dr. Zuzana Hlavenkova for acquiring STEM-EDS micrographs and Dr. François Devred for assistance on the DRUV-Vis measurements. We also thank Prof. Christophe Copéret for his constructive and insightful suggestions. Plaifa Hongmanorom also acknowledges the support of the Fonds De La Recherche Scientifique – FNRS (10.13039/501100002661) for her postdoctoral researcher – CR fellowship. DPD thanks the Francqui Foundation for the Francqui Research Professor chair.

References

[1] A. George, B. Shen, M. Craven, Y. Wang, D. Kang, C. Wu, X. Tu, A Review of Non-Thermal Plasma Technology: A novel solution for CO2 conversion and utilization, Renew. Sustain. Energy Rev., 135 (2021) 109702.

[2] M.M.F. Hasan, L.M. Rossi, D.P. Debecker, K.C. Leonard, Z. Li, B.C.E. Makhubela, C. Zhao, A. Kleij, Can CO2 and Renewable Carbon Be Primary Resources for Sustainable Fuels and Chemicals?, ACS Sustainable Chemistry & Engineering, 9 (2021) 12427-12430.

[3] M. Götz, J. Lefebvre, F. Mörs, A. McDaniel Koch, F. Graf, S. Bajohr, R. Reimert, T. Kolb, Renewable Power-to-Gas: A technological and economic review, Renewable Energy, 85 (2016) 1371-1390.

[4] M. Thema, F. Bauer, M. Sterner, Power-to-Gas: Electrolysis and methanation status review, Renew. Sustain. Energy Rev., 112 (2019) 775-787.

[5] S. Roy, A. Cherevotan, S.C. Peter, Thermochemical CO2 Hydrogenation to Single Carbon Products: Scientific and Technological Challenges, ACS Energy Letters, 3 (2018) 1938-1966.

[6] L. Shen, J. Xu, M. Zhu, Y.-F. Han, Essential Role of the Support for Nickel-Based CO2 Methanation Catalysts, ACS Catal., 10 (2020) 14581-14591.

[7] J. Ashok, S. Pati, P. Hongmanorom, Z. Tianxi, C. Junmei, S. Kawi, A review of recent catalyst advances in CO2 methanation processes, Catal. Today, 356 (2020) 471-489.

[8] R. Dębek, F. Azzolina-Jury, A. Travert, F. Maugé, A review on plasma-catalytic methanation of carbon dioxide – Looking for an efficient catalyst, Renew. Sustain. Energy Rev., 116 (2019) 109427.
[9] Y. Guo, S. Mei, K. Yuan, D.-J. Wang, H.-C. Liu, C.-H. Yan, Y.-W. Zhang, Low-Temperature CO2 Methanation over CeO2-Supported Ru Single Atoms, Nanoclusters, and Nanoparticles Competitively Tuned by Strong Metal–Support Interactions and H-Spillover Effect, ACS Catal., 8 (2018) 6203-6215.
[10] J.H. Kwak, L. Kovarik, J. Szanyi, CO2 Reduction on Supported Ru/Al2O3 Catalysts: Cluster Size Dependence of Product Selectivity, ACS Catal., 3 (2013) 2449-2455.
[11] Z. Kowalczyk, K. Stołecki, W. Raróg-Pilecka, E. Miśkiewicz, E. Wilczkowska, Z. Karpiński, Supported ruthenium catalysts for selective methanation of carbon oxides at very low COx/H2 ratios, Appl. Catal., A, 342 (2008) 35-39.
[12] A. Kim, D.P. Debecker, F. Devred, V. Dubois, C. Sanchez, C. Sassoye, CO2 methanation on Ru/TiO2 catalysts: On the effect of mixing anatase and rutile TiO2 supports, Appl. Catal., B, 220 (2018) 615-625.
[13] J.A.H. Dreyer, P. Li, L. Zhang, G.K. Beh, R. Zhang, P.H.L. Sit, W.Y. Teoh, Influence of the oxide support reducibility on the CO2 methanation over Ru-based catalysts, Appl. Catal., B, 219 (2017) 715-726.
[14] A. Aitbekova, L. Wu, C.J. Wrasman, A. Boubnov, A.S. Hoffman, E.D. Goodman, S.R. Bare, M. Cargnello, Low-Temperature Restructuring of CeO2-Supported Ru Nanoparticles Determines Selectivity in CO2 Catalytic Reduction, Journal of the American Chemical Society, 140 (2018) 13736-13745.
[15] J. Zhou, Z. Gao, G. Xiang, T. Zhai, Z. Liu, W. Zhao, X. Liang, L. Wang, Interfacial compatibility critically controls Ru/TiO2 metal-support interaction modes in CO2 hydrogenation, Nature Communications, 13 (2022) 327.
[16] A.M. Abdel-Mageed, K. Wiese, M. Parlinska-Wojtan, J. Rabeah, A. Brückner, R.J. Behm, Encapsulation of Ru nanoparticles: Modifying the reactivity toward CO and CO2 methanation on highly active Ru/TiO2 catalysts, Appl. Catal., B, 270 (2020) 118846.
[17] D. Li, N. Ichikuni, S. Shimazu, T. Uematsu, Catalytic properties of sprayed Ru/Al2O3 and promoter effects of alkali metals in CO2 hydrogenation, Appl. Catal., A, 172 (1998) 351-358.
[18] A. Petala, P. Panagiotopoulou, Methanation of CO2 over alkali-promoted Ru/TiO2 catalysts: I. Effect of alkali additives on catalytic activity and selectivity, Appl. Catal., B, 224 (2018) 919-927.
[19] P. Panagiotopoulou, Methanation of CO2 over alkali-promoted Ru/TiO2 catalysts: II. Effect of alkali additives on the reaction pathway, Appl. Catal., B, 236 (2018) 162-170.
[20] M. Gao, J. Zhang, P. Zhu, X. Liu, Z. Zheng, Unveiling the origin of alkali metal promotion in CO2 methanation over Ru/ZrO2, Appl. Catal., B, 314 (2022) 121476.
[21] S. Cisneros, L. Santa-Taborda, L. Martínez Quintana, A.I.M. Rabee, H. Abed, N. Rockstroh, S. Bartling, M. Romero-Sáez, H. Atia, A. Belén Dongil, A. Brückner, J. Rabeah, The effect of O-vacancies on intermediates stability and electron delocalization over MgO modified Ru/ZrO2: Spectroscopic insights during CO2 methanation, Chem. Eng. J., 474 (2023) 145646.
[22] S. Tada, O.J. Ochieng, R. Kikuchi, T. Haneda, H. Kameyama, Promotion of CO2 methanation activity and CH4 selectivity at low temperatures over Ru/CeO2/Al2O3 catalysts, Int. J. Hydrogen Energy, 39 (2014) 10090-10100.
[23] X. Xu, L. Liu, Y. Tong, X. Fang, J. Xu, D.-e. Jiang, X. Wang, Facile Cr3+-Doping Strategy Dramatically Promoting Ru/CeO2 for Low-Temperature CO2 Methanation: Unraveling the Roles of Surface Oxygen Vacancies and Hydroxyl Groups, ACS Catal., 11 (2021) 5762-5775.
[24] R.C. Rabelo-Neto, M.P. Almeida, E.B. Silveira, M. Ayala, C.D. Watson, J. Villarreal, D.C. Cronauer, A.J. Kropf, M. Martinelli, F.B. Noronha, G. Jacobs, CO2 hydrogenation: Selectivity control of CO versus CH4 achieved using Na doping over Ru/m-ZrO2 at low pressure, Appl. Catal., B, 315 (2022) 121533.
[25] S. Cisneros, S. Chen, C. Fauth, A.M. Abdel-Mageed, S. Pollastri, J. Bansmann, L. Olivi, G. Aquilanti, H. Atia, J. Rabeah, M. Parlinska-Wojtan, A. Brückner, R.J. Behm, Controlling the selectivity of high-surface-area Ru/TiO2 catalysts in CO2 reduction - modifying the reaction properties by Si doping of the support, Appl. Catal., B, 317 (2022) 121748.

[26] P. Hongmanorom, V. Smeets, A. Neraud, A. Styskalik, P. Praserthdam, C. Copéret, D.P. Debecker, Promotional effect of Ti on mesoporous silica-supported Ru catalysts for CO2 methanation, Materials Today Chemistry, 49 (2025) 103026.
[27] Y. Yu, Z. Bian, Z. Wang, J. Wang, W. Tan, Q. Zhong, S. Kawi, CO2 methanation on Ni-Ce0.8M0.2O2 (M=Zr, Sn or Ti) catalyst: Suppression of CO via formation of bridging carbonyls on nickel, Catal. Today, 424 (2023) 113053.
[28] G. Garbarino, P. Kowalik, P. Riani, K. Antoniak-Jurak, P. Pieta, A. Lewalska-Graczyk, W. Lisowski, R. Nowakowski, G. Busca, I.S. Pieta, Improvement of Ni/Al2O3 Catalysts for Low-Temperature CO2 Methanation by Vanadium and Calcium Oxide Addition, Industrial & Engineering Chemistry Research, 60 (2021) 6554-6564.
[29] X. Zou, Y. Meng, J. Liu, Y. Cao, L. Cui, Z. Shen, Q. Xia, X. Li, S. Zhang, Z. Ge, Y. Pan, Y. Wang, Niobium Modification of CeO2 Tuning Electron Density of Nickel–Ceria Interfacial Sites for Enhanced CO2 Methanation, Inorg. Chem., 63 (2024) 881-890.
[30] T.A. Le, J. Kim, J.K. Kang, E.D. Park, CO and CO2 methanation over M (MMn, Ce, Zr, Mg, K, Zn, or V)-promoted Ni/Al@Al2O3 catalysts, Catal. Today, 348 (2020) 80-88.
[31] V. Smeets, C. Boissière, C. Sanchez, E.M. Gaigneaux, E. Peeters, B.F. Sels, M. Dusselier, D.P. Debecker, Aerosol Route to TiO2–SiO2 Catalysts with Tailored Pore Architecture and High Epoxidation Activity, Chem. Mater., 31 (2019) 1610-1619.
[32] S. Pega, C. Boissière, D. Grosso, T. Azaïs, A. Chaumonnot, C. Sanchez, Direct Aerosol Synthesis of Large-Pore Amorphous Mesostructured Aluminosilicates with Superior Acid-Catalytic Properties, Angew. Chem. Int. Ed., 48 (2009) 2784-2787.
[33] H. Yang, Q. Lu, F. Gao, Q. Shi, Y. Yan, F. Zhang, S. Xie, B. Tu, D. Zhao, One-Step Synthesis of Highly Ordered Mesoporous Silica Monoliths with Metal Oxide Nanocrystals in their Channels, Adv. Funct. Mater., 15 (2005) 1377-1384.
[34] R. De Clercq, M. Dusselier, C. Poleunis, D.P. Debecker, L. Giebeler, S. Oswald, E. Makshina, B.F. Sels, Titania-Silica Catalysts for Lactide Production from Renewable Alkyl Lactates: Structure–Activity Relations, ACS Catal., 8 (2018) 8130-8139.
[35] J. Lu, K.M. Kosuda, R.P. Van Duyne, P.C. Stair, Surface Acidity and Properties of TiO2/SiO2 Catalysts Prepared by Atomic Layer Deposition: UV–visible Diffuse Reflectance, DRIFTS, and Visible Raman Spectroscopy Studies, J. Phys. Chem. C, 113 (2009) 12412-12418.
[36] B. Tang, W. Dai, X. Sun, G. Wu, N. Guan, M. Hunger, L. Li, Mesoporous Zr-Beta zeolites prepared by a post-synthetic strategy as a robust Lewis acid catalyst for the ring-opening aminolysis of epoxides, Green Chem., 17 (2015) 1744-1755.
[37] S.-Y. Chen, J.-F. Lee, S. Cheng, Pinacol-type rearrangement catalyzed by Zr-incorporated SBA-15, J. Catal., 270 (2010) 196-205.
[38] J. Iglesias, J.A. Melero, L.F. Bautista, G. Morales, R. Sánchez-Vázquez, M.T. Andreola, A. Lizarraga-Fernández, Zr-SBA-15 as an efficient acid catalyst for FAME production from crude palm oil, Catal. Today, 167 (2011) 46-55.
[39] H. Berndt, A. Martin, A. Brückner, E. Schreier, D. Müller, H. Kosslick, G.U. Wolf, B. Lücke, Structure and Catalytic Properties of VOx/MCM Materials for the Partial Oxidation of Methane to Formaldehyde, J. Catal., 191 (2000) 384-400.
[40] P. Hu, W.-Z. Lang, X. Yan, X.-F. Chen, Y.-J. Guo, Vanadium-doped porous silica materials with high catalytic activity and stability for propane dehydrogenation reaction, Appl. Catal., A, 553 (2018) 65-73.
[41] Y.-M. Liu, Y. Cao, N. Yi, W.-L. Feng, W.-L. Dai, S.-R. Yan, H.-Y. He, K.-N. Fan, Vanadium oxide supported on mesoporous SBA-15 as highly selective catalysts in the oxidative dehydrogenation of propane, J. Catal., 224 (2004) 417-428.
[42] E.L. Lee, I.E. Wachs, In Situ Spectroscopic Investigation of the Molecular and Electronic Structures of SiO2 Supported Surface Metal Oxides, J. Phys. Chem. C, 111 (2007) 14410-14425.

[43] L.C. Kao, W.C. Kan, R.M. Martin-Aranda, M.O. Guerrero-Perez, M.Á. Bañares, S.Y.H. Liou, SiO2 supported niobium oxides with active acid sites for the catalytic acetalization of glycerol, Catal. Today, 356 (2020) 80-87.
[44] S. Esposito, B. Silvestri, C. Rossano, V. Vermile, C. Imparato, M. Manzoli, B. Bonelli, V. Russo, E.M. Gaigneaux, A. Aronne, M. Di Serio, The role of metallic and acid sites of Ru-Nb-Si catalysts in the transformation of levulinic acid to γ-valerolactone, Appl. Catal., B, 310 (2022) 121340.
[45] T.N. Phaahlamohlaka, D.O. Kumi, M.W. Dlamini, R. Forbes, L.L. Jewell, D.G. Billing, N.J. Coville, Effects of Co and Ru Intimacy in Fischer–Tropsch Catalysts Using Hollow Carbon Sphere Supports: Assessment of the Hydrogen Spillover Processes, ACS Catal., 7 (2017) 1568-1578.
[46] Y. Zhang, L. Li, F. Liu, H. Qi, L. Zhang, W. Guan, Y. Liu, A. Wang, T. Zhang, Synergy between Ru and WOx Enables Efficient Hydrodeoxygenation of Primary Amides to Amines, ACS Catal., 12 (2022) 6302-6312.
[47] C. Fernández, N. Bion, E.M. Gaigneaux, D. Duprez, P. Ruiz, Kinetics of hydrogen adsorption and mobility on Ru nanoparticles supported on alumina: Effects on the catalytic mechanism of ammonia synthesis, J. Catal., 344 (2016) 16-28.
[48] N. Yan, W. Chen, J. Chen, Z. Qu, Y. Guo, S. Yang, J. Jia, Significance of RuO2 Modified SCR Catalyst for Elemental Mercury Oxidation in Coal-fired Flue Gas, Environ. Sci. Technol., 45 (2011) 5725-5730.
[49] S. Carenco, C. Sassoye, M. Faustini, P. Eloy, D.P. Debecker, H. Bluhm, M. Salmeron, The Active State of Supported Ruthenium Oxide Nanoparticles during Carbon Dioxide Methanation, J. Phys. Chem. C, 120 (2016) 15354-15361.
[50] R. Bulánek, P. Čičmanec, H. Sheng-Yang, P. Knotek, L. Čapek, M. Setnička, Effect of preparation method on nature and distribution of vanadium species in vanadium-based hexagonal mesoporous silica catalysts: Impact on catalytic behavior in propane ODH, Appl. Catal., A, 415-416 (2012) 29-39.
[51] G. Rampelberg, B. De Schutter, W. Devulder, K. Martens, I. Radu, C. Detavernier, In situ X-ray diffraction study of the controlled oxidation and reduction in the V–O system for the synthesis of VO2 and V2O3 thin films, Journal of Materials Chemistry C, 3 (2015) 11357-11365.
[52] S.A. Corr, M. Grossman, J.D. Furman, B.C. Melot, A.K. Cheetham, K.R. Heier, R. Seshadri, Controlled Reduction of Vanadium Oxide Nanoscrolls: Crystal Structure, Morphology, and Electrical Properties, Chem. Mater., 20 (2008) 6396-6404.
[53] A.G. Sato, D.P. Volanti, D.M. Meira, S. Damyanova, E. Longo, J.M.C. Bueno, Effect of the ZrO2 phase on the structure and behavior of supported Cu catalysts for ethanol conversion, J. Catal., 307 (2013) 1-17.
[54] T.H. Vuong, J. Radnik, E. Kondratenko, M. Schneider, U. Armbruster, A. Brückner, Structure-reactivity relationships in VOx/CexZr1−xO2 catalysts used for low-temperature NH3-SCR of NO, Appl. Catal., B, 197 (2016) 159-167.
[55] D.P. Debecker, K. Bouchmella, R. Delaigle, P. Eloy, C. Poleunis, P. Bertrand, E.M. Gaigneaux, P.H. Mutin, One-step non-hydrolytic sol–gel preparation of efficient V2O5-TiO2 catalysts for VOC total oxidation, Appl. Catal., B, 94 (2010) 38-45.
[56] Z. Song, Y. Peng, X. Zhao, H. Liu, C. Gao, W. Si, J. Li, Roles of Ru on the V2O5–WO3/TiO2 Catalyst for the Simultaneous Purification of NOx and Chlorobenzene: A Dechlorination Promoter and a Redox Inductor, ACS Catal., 12 (2022) 11505-11517.
[57] S.N. Birajdar, N.Y. Hebalkar, S.K. Pardeshi, S.K. Kulkarni, P.V. Adhyapak, Ruthenium-decorated vanadium pentoxide for room temperature ammonia sensing, RSC Adv., 9 (2019) 28735-28745.
[58] E.V. Kondratenko, M. Cherian, M. Baerns, D. Su, R. Schlögl, X. Wang, I.E. Wachs, Oxidative dehydrogenation of propane over V/MCM-41 catalysts: comparison of O2 and N2O as oxidants, J. Catal., 234 (2005) 131-142.
[59] Z. Wu, P.C. Stair, S. Rugmini, S.D. Jackson, Raman Spectroscopic Study of V/θ-Al2O3 Catalysts: Quantification of Surface Vanadia Species and Their Structure Reduced by Hydrogen, J. Phys. Chem. C, 111 (2007) 16460-16469.

[60] S. Keilholz, R. Paul, L.Y. Dorsch, H. Kohlmann, In Situ X-ray Diffraction Studies on the Reduction of V2O5 and WO3 by Using Hydrogen, Chemistry – A European Journal, 29 (2023) e202203932.
[61] J. Xu, X. Su, H. Duan, B. Hou, Q. Lin, X. Liu, X. Pan, G. Pei, H. Geng, Y. Huang, T. Zhang, Influence of pretreatment temperature on catalytic performance of rutile TiO2-supported ruthenium catalyst in CO2 methanation, J. Catal., 333 (2016) 227-237.
[62] S. Chen, A.M. Abdel-Mageed, M. Li, S. Cisneros, J. Bansmann, J. Rabeah, A. Brückner, A. Groß, R.J. Behm, Electronic metal-support interactions and their promotional effect on CO2 methanation on Ru/ZrO2 catalysts, J. Catal., 400 (2021) 407-420.
[63] J. Li, Z. Liu, D.A. Cullen, W. Hu, J. Huang, L. Yao, Z. Peng, P. Liao, R. Wang, Distribution and Valence State of Ru Species on CeO2 Supports: Support Shape Effect and Its Influence on CO Oxidation, ACS Catal., 9 (2019) 11088-11103.
[64] Y. Yan, Q. Wang, C. Jiang, Y. Yao, D. Lu, J. Zheng, Y. Dai, H. Wang, Y. Yang, Ru/Al2O3 catalyzed CO2 hydrogenation: Oxygen-exchange on metal-support interfaces, J. Catal., 367 (2018) 194-205.
[65] M. Liu, R. Zou, C.-j. Liu, Improvement in the activity of Ru/ZrO2 for CO2 methanation by the enhanced hydrophilicity of zirconia, Applied Catalysis B: Environment and Energy, 360 (2025) 124549.
[66] S. Cisneros, A. Abdel-Mageed, J. Mosrati, S. Bartling, N. Rockstroh, H. Atia, H. Abed, J. Rabeah, A. Brückner, Oxygen vacancies in Ru/TiO2 - drivers of low-temperature CO2 methanation assessed by multimodal operando spectroscopy, iScience, 25 (2022) 103886.